JOURNAL OF GUIDANCE, CONTROL, AND DYNAMICS
Vol. 29, No. 4, July–August 2006

Trajectory Tracking Controller for Vision-Based Probe and Drogue Autonomous Aerial Refueling

Monish D. Tandale, Roshawn Bowers, and John Valasek
Texas A&M University, College Station, Texas 77843-3141

Practical autonomous aerial refueling between unmanned tanker and receiver aircraft using the probe-and-drogue method requires a reliable relative position sensor integrated with a robust relative navigation and control algorithm. The system must provide successful docking in the presence of disturbances caused by both the tanker wake vortex and atmospheric turbulence. This paper develops a reference-observer-based tracking controller and integrates it with an existing vision-based relative navigation sensor. Relative drogue position measured by the sensor is transformed into a smooth reference trajectory generated onboard the receiver aircraft in real time, and an output injection observer estimates the feedforward control and the reference states to be tracked. Accurate tracking is provided by a state feedback controller with good disturbance rejection properties. A frequency-domain stability analysis for the combined reference observer and controller shows robustness to sensor noise, atmospheric turbulence, and high-frequency unmodeled dynamics. Feasibility and performance are demonstrated by simulated docking maneuvers with a nonstationary drogue in the tanker flowfield, subjected to various levels of atmospheric turbulence. Results presented in the paper show that the integrated sensor and controller enable precise aerial refueling, including consideration of realistic sensor measurements errors, plant modeling errors, and disturbances.

Monish D. Tandale from Mumbai, India earned the Bachelor of Engineering Degree (B.E.) with distinction from Victoria Jubilee Technical Institute, University of Mumbai in 2000, and the M.S. and Ph.D. degrees in aerospace engineering from Texas A&M University in 2002 and 2006 respectively. As a graduate research assistant in the Flight Simulation Laboratory, he has worked on fighter agility metrics, fault tolerant adaptive control, and vision-based navigation systems. He is a recipient of the Regents Graduate Fellowship and was a finalist for the 2003 Eppright Outstanding International Student Award. Since February 2006 he has been a research scientist at Optimal Synthesis, Palo Alto, California. His research interests include autonomous aerial refueling, fault-tolerant adaptive control, adaptive control in the presence of actuator saturation, and intelligent control of morphing aircraft. monish@optisyn.com. Member AIAA.

Roshawn Bowers earned the B.S. (2002) and M.S (2005) in aerospace engineering from Texas A&M University. She has served two successive Co-Op tours with Lockheed Martin Space Operations, Houston, Texas (2000), a summer graduate internship with Lockheed Martin Aeronautics, Fort Worth, Texas (2003), and a graduate fellow internship with the Central Intelligence Agency, Langley, Virginia (2004). As a graduate research assistant she researched vision-based navigation systems for autonomous vehicles, and as an undergraduate in the Engineering Scholars Program, she researched automatic carrier landing systems and flight tested an autonomous powered parafoil vehicle for NASA's X-38 project. She is a recipient of the Texas A&M University Graduate Merit Fellowship and the Dean's Honor Award from the Dwight Look College of Engineering. She is a four-time recipient of the Isadore Roosth '33 Engineering Scholarship. She has also served as the chairperson of the Texas A&M Chapter of Sigma Gamma Tau, the aerospace engineering honor society. Since May of 2005 she has been an engineer working in the Vehicle Management Systems and Flight Controls group at Northrop Grumman Integrated Systems in El Segundo, California. Her research interests include vision-based navigation and control, formation flight, and unmanned aerial vehicles. roshawn.bowers@ngc.com. Member AIAA.

John Valasek earned the B.S. degree in aerospace engineering from California State Polytechnic University, Pomona in 1986 and the M.S. degree with honors and the Ph.D. in aerospace engineering from the University of Kansas, in 1991 and 1995, respectively. He was a flight control engineer for the Northrop Corporation, Aircraft Division from 1985 to 1988, where he worked in the Flight Controls Research Group, and on the AGM-137 Tri-Services Standoff Attack Missile (TSSAM) program. He previously held an academic appointment at Western Michigan University (1995-1997), was a summer faculty researcher at NASA Langley (1996), and an AFOSR Summer Faculty Research Fellow at the Air Force Research Laboratory (1997). Since then he has been with Texas A&M University, where he is Associate Professor of Aerospace Engineering, and Director of the Flight Simulation Laboratory. He teaches courses on vehicle management systems, digital control, nonlinear systems, flight mechanics, and cockpit systems and displays. He also co-teaches a short course on digital flight control for the University of Kansas Division of Continuing Education. Current research interests include control of morphing air and space vehicles, multi-agent systems, intelligent autonomous control, vision-based navigation systems, and fault tolerant adaptive control. From 2005 to 2006 he served on both the Steering Committee and on the Guidance, Navigation, and Control Panel of a National Research Council Decadal Survey of Civil Aeronautics Research. He is an Associate Fellow of AIAA, past Chairman and current member of the Atmospheric Flight Mechanics Technical Committee, General Chair of the 1998 Atmospheric Flight Mechanics Conference, Technical Chair of the 1999 Atmospheric Flight Mechanics Conference, and current member of the General Aviation Systems Technical Committee. valasek@tamu.edu http:// jungfrau.tamu.edu/valasek/.

Presented as Paper 2005-5868 at the Guidance, Navigation, and Control Conference, San Francisco, CA, 15–18 August 2005; received 25 August 2005; revision received 11 November 2005; accepted for publication 30 November 2005.

I. Introduction

AUTONOMOUS in-flight aerial refueling is an important capability for the future deployment of unmanned aerial vehicles.[1,2] Reference 2 provides an overview of the various aspects of aerial refuelling for unmanned aerial vehicles. Boom-and-receptacle and probe-and-drogue are the hardware configurations and methods commonly used for aerial refueling. In the former, a refueling boom on the rear of the tanker aircraft is steered into the refueling port on the receiver aircraft. In this method, the job of the receiver aircraft is to maintain proper position with respect to the tanker. With the probe-and-drogue method, the tanker aircraft trails a hose with an aerodynamically stabilized flexible "basket" or drogue. The receiver aircraft has a probe that must be placed or docked into the drogue. This is the preferred method for small, agile aircraft because the equipment is small and lightweight, and a human operator is not required on the tanker aircraft. This is the refueling method considered in the present research.

Several approaches to the control aspect of autonomous aerial refueling (AAR) have been investigated in combination with various sensor systems. Successful refueling operation requires guidance laws for rendezvous[3] and accurate control laws for docking once the aircraft are in close proximity. Campa et al.[4,5] proposed a robust linear quadratic regulator (LQR) and H_∞ controller, which tracks a reference signal from a fuzzy fusion of measurements from the global-positioning system (GPS) and an artificial vision sensor. They included a finite element model of a flexible "boom-drogue" in Dryden moderate turbulence.[4,5] Accurate tracking performance was demonstrated using nonlinear simulation, but the resulting controller is 24th order. Stepanyan et al. considered the problem of autonomous air refueling autopilot design using techniques from differential games and adaptive control.[6] An adaptive control signal was used for the compensation of vortex induced uncertainties. The availability of perfect measurements was assumed without a true relative navigation sensor in the loop. Simulations were considered only for the longitudinal dynamics of the aircraft. Pachter et al. used quantitative feedback theory to design an automatic stationkeeping fight control system for regulating the position of an aircraft receiving fuel relative to the tanker aircraft during air-to-air refueling, assuming that a relative navigation sensor was available.[7] Pollini et al.[8] have developed an artificial vision system for relative position estimation, based on localization of passive infrared markers, which have a known geometry distribution over the leader airframe or drogue body. Simulations of refueling scenarios with the sensor in the loop were not performed. Valasek et al.[9] and Kimmett et al.[10] proposed an optimal nonzero set point with control rate weighting (NZSP-CRW) control structure to track and dock with a stationary drogue in Dryden light turbulence using a cooperative vision-based sensor. This work was extended to a moving drogue using the command-generator-tracker (CGT) control scheme, in which a reference trajectory is generated by a model of the drogue with known inputs.[11] The main drawback to both nonzero set point and CGT is that the position or trajectory of the drogue is assumed to be known a priori, and an accurate model of the drogue dynamics is required.

This paper extends and improves the earlier work done by the authors in Ref. 1 by developing a reference-observer-based tracking controller (ROTC), which does not require a drogue model or presumed knowledge of the drogue position. The original contribution of this paper is the use of a reference observer to estimate the open-loop feedforward control and the reference states that the plant needs to follow, so as to track a reference trajectory generated onboard the aircraft in real time. The only inputs to the control structure are the relative positions between the probe and the drogue as measured by a vision-based sensor. The previously used NZSP-CRW-based controller assumes a steady drogue position and neglects the state derivative while estimating the state and the control. The ROTC controller developed here incorporates the state derivative in the estimation process and hence does not exhibit significant lag in the tracking performance. When combined with the robust controller, the feasible reference trajectories generated in this manner produce high docking success rates in the presence of tanker wake vortex effects and higher levels of atmospheric turbulence, which the NZSP-CRW controller is not able to provide.

The paper is organized as follows. Section II describes the VisNav vision-based sensor and its measurements. The ROTC is then developed in three sections. Section III develops the reference trajectory generator, which uses VisNav measurements as its input. Section IV develops the observer that estimates the plant states and controls that the plant needs to follow, to achieve the desired reference trajectory, and Sec. V develops the trajectory tracking state feedback controller that accurately tracks these states to achieve precise docking even in the presence of turbulence and disturbances caused by the tanker vortex wake. Section VI presents a frequency-domain stability robustness and performance robustness analysis of the controller. Section VII contains a simulation example consisting of a docking maneuver in light turbulence, an investigation of VisNav sensor performance characteristics using the simulation, and a performance comparison between the ROTC system developed in this paper, and the earlier controller of Ref. 1. Conclusions and recommendations for future research are presented in Sec. VIII, and the appendix contains details of the receiver aircraft model.

II. Vision-Based Navigation Sensor

A critical technology for autonomous aerial refueling is an adequate sensor for measuring the relative position and orientation between the receiver aircraft and the tanker aircraft. The rapid control corrections needed for docking, especially in turbulence, require accurate high-frequency navigation updates. Some methods that have been considered for determining relative position in a refueling scenario include the GPS and visual servoing with pattern recognition software.[12–16] GPS measurements have been made with 1- to 2-cm accuracy for formation flying, but problems associated with lock-on, integer ambiguity, and low bandwidth present challenges for application to in-flight refueling. Pattern recognition codes are not reliable in all lighting conditions and, with adequate fault tolerance, might require large amounts of computational power to converge with sufficient confidence to a solution.[12–14] Reference 1 introduced a candidate vision-based navigation system called VisNav, which provides high-precision, six-degrees-of-freedom information for real-time navigation applications. It is a vision-based sensor that offers the accuracy and reliability needed for the in-flight refueling task, and its small size and low power requirements make it suitable for most UAV platforms.

VisNav provides a six-degrees-of-freedom navigation solution composed of the relative position and orientation between two vehicles or objects. It works by measuring the line-of-sight (LOS) vectors between the sensor, which is mounted on one vehicle, and a set of structured light beacons that are rigidly attached to the target vehicle. Because the beacons have a known position in the target vehicle frame, it is possible to recover the relative position and orientation of the sensor with respect to the target frame.

Figure 1 shows the Version 3.2 VisNav sensor. The sensor component of the system contains a position-sensing diode (PSD), a wide-angle lens, and a digital signal processor (DSP). A beacon controller mounted on the receiver aircraft orchestrates the sequence and timing of the beacons' activation. It communicates with the beacons through an infrared or radio data link. The beacon controller also uses feedback control to hold the beacon light intensity at about 70% of the saturation level of the PSD. This prevents damage to the photo diode and maintains an optimal signal-to-noise ratio throughout operation.[1]

When VisNav is operating, the DSP commands the beacon controller to signal each beacon to activate in turn. As each beacon turns on, light comes through the wide-angle lens and is focused onto the PSD. The focused light creates a centroid, or spot, on the photo diode, which causes a current imbalance in the four terminals on each side of the PSD, as shown in Fig. 2. The closer the light centroid is to one side of the photo diode, the higher the current in the nearest terminal. By measuring the voltage at each terminal, the two-dimensional position of the light centroid on the PSD can be found with a nonlinear calibration function. From these measurements, unit LOS vectors from the sensor to each

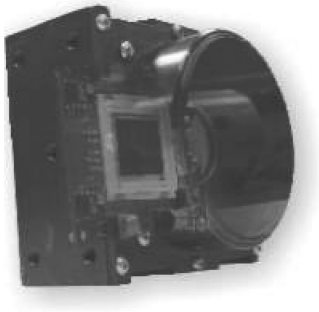

a) VisNav sensor box

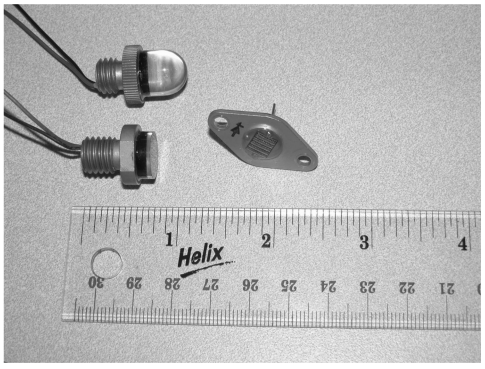

b) Light-emitting-diode beacons

Fig. 1 VisNav 3.2 hardware components.

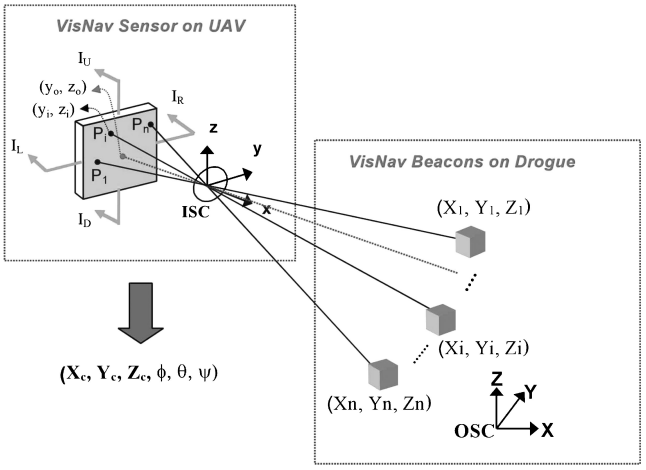

Fig. 2 VisNav sensor model.

beacon can be determined. Once measurements from four or more beacons are collected, they are passed to a Gaussian least-squares differential-correction (GLSDC) algorithm. This routine calculates the minimum-variance estimate of the position and orientation of the sensor relative to the target frame.

Figure 3 shows a VisNav mobile platform docking demonstrator. It was created for development and evaluation of the VisNav system hardware, and a primary objective is to demonstrate feasibility and performance of the sensor in outdoor lighting conditions. The mobile platform is also the basis for an air-to-air demonstration of autonomous probe and drogue air refueling. It mimics the receiver aircraft and docks with a semirigid refuelling drogue mounted on a test stand that mimics the tanker aircraft. The horizontal rod seen at the top is a full-scale nonfunctioning test article of a refueling probe designed for small aircraft or UAVs. The mobile platform has three-degrees-of-freedom in the horizontal plane: two translational and one rotational. The VisNav sensor is mounted at the intersection of the refueling probe and the vertical support; the beacons are attached to the drogue. Numerous docking runs were successfully

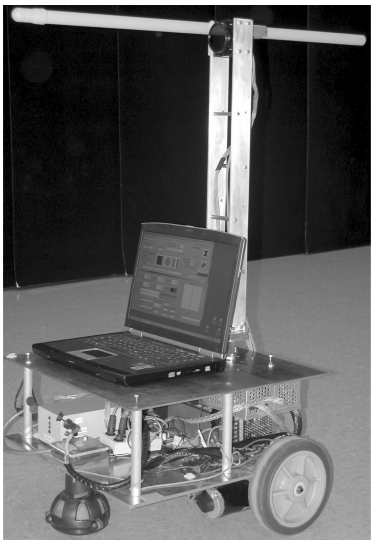

Fig. 3 VisNav mobile platform docking demonstrator.

Fig. 4 Candidate beacon configuration for AAR, as seen from VisNav sensor.

performed in outdoor lighting conditions of bright sunlight to validate the sensor.

For the research presented in this paper, the active beacon array is located on the refueling drogue (Fig. 4). Only four beacons are required to obtain a unique six-degrees-of-freedom navigation solution. In the GLSDC measurement model there are six unknowns, the three relative positions and three relative orientation coordinates. Each available beacon contributes two measurement equations, one for each two-dimensional coordinate of its projection on the PSD. It follows that measurements from at least three beacons must be obtained before the system of equations can be solved. However, the geometry of three beacons alone is not unique, such that there are some configurations of three beacons which project identically onto the two-dimensional plane. Only with measurements from four or more beacons is a unique solution ensured. Earlier work by the authors on GLSDC development shows that nonlinear least squares (also known as GLSDC) finds the best-fit solution for a given set of measurements and an assumed amount of measurement noise.[1] Using more than four beacons provides robustness to measurement noise, but also adds computational expense. A set of eight beacons provides a good balance between these two factors for the AAR application.[17] When measurement noise is accounted for, it is the quality of the geometry (the three-dimensional arrangement of the beacons) and not the number of beacons that determines the accuracy of the pose estimate at a given range. This provides redundancy in case a beacon falls outside of the field of view, and the additional measurements improve the convergence performance of the estimation routine. A second set of beacons that are close together can then be used for close-proximity navigation. A desirable configuration ensures that the lateral extent of the beacon array takes up at least 10% of the sensor field of view within the range of interest.[18]

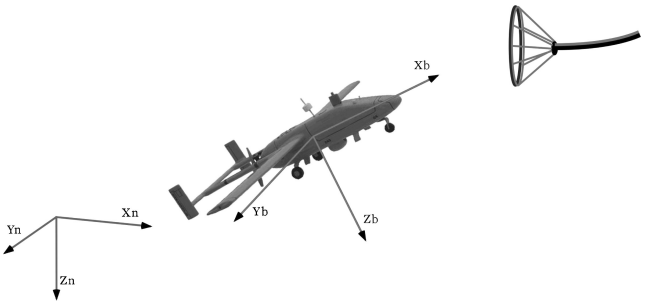

Fig. 5 Axis system.

III. Reference Trajectory Generation

Consider the axis system shown in Fig. 5. The Earth-fixed inertial axis system (X_n,Y_n,Z_n) is oriented with the X_n axis pointing along the heading of both the tanker and receiver aircraft, and the Z_n axis points in the direction of gravity. The body axis (X_b,Y_b,Z_b) is attached to the receiver aircraft with the origin at its center of gravity.

Let (X_d,Y_d,Z_d) be the initial offset as measured along the inertial axis, between the mean position of the refueling drogue and the probe attached to the receiver aircraft. The drogue exhibits random oscillatory behavior in the plane parallel to the (Y_n,Z_n) plane, and its mean position can be estimated by taking an average of the drogue position over a period of 10 s prior to initiating the docking maneuver. Note that the drogue is also perturbed in translation along the direction of flight, but the magnitude of these perturbations is small. The drogue is also subjected to angular perturbations that disturb its orientation.

It is a common practice followed by human pilots to line up behind the drogue initially in the (Y_n,Z_n) plane and then dock with the drogue by advancing ahead along X_n. Following a similar technique, the reference trajectory is designed in two stages. In the first stage, the refueling probe on the receiver aircraft tries to line up behind the mean position of the drogue so that the initial offset (Y_d,Z_d) becomes zero. A fifth-order polynomial was used to design the flight trajectory so that the boundary conditions can be imposed to preserve continuity in the position, velocity, and acceleration states at both the end points of the trajectory. The continuity in acceleration enforces continuity in the desired control effort. With a third-order polynomial, continuity can be enforced in the position and velocity level states only. The authors chose to use a fifth-order polynomial as it makes the trajectory transitions smoother without a significant increase in the computational load.

Consider only the offset along the Y_n axis for simplicity. At the beginning of stage 1, the reference trajectory is steady level 1-g flight. The perturbations in reference position, velocity, and acceleration are zero at the initial time t_0. For the final time t_1 of stage 1, the reference position is Y_d, and the velocity and acceleration are zero. Let $y_r(t)$ be the coordinate of the reference trajectory along the Y_n axis. Using a fifth-order polynomial, $y_r(t)$ can be written as

$$y_r(t) = y_0 + y_1 t + y_2 t^2 + y_3 t^3 + y_4 t^4 + y_5 t^5, \quad \text{if} \quad t \le t_1 \tag{1}$$

The parameters $y_0 \cdots y_5$ can be calculated by imposing the following boundary conditions:

$$y_r(t) = 0, \quad \frac{\mathrm{d}y_r}{\mathrm{d}t}(t) = 0, \quad \frac{\mathrm{d}^2 y_r}{\mathrm{d}t^2}(t) = 0 \quad \text{at} \quad t = 0$$

$$y_r(t) = Y_d, \quad \frac{\mathrm{d}y_r}{\mathrm{d}t}(t) = 0, \quad \frac{\mathrm{d}^2 y_r}{\mathrm{d}t^2}(t) = 0 \quad \text{at} \quad t = t1 \tag{2}$$

$z_r(t)$ for stage 1 can be calculated in a similar manner. The reference trajectory that zeros the offset X_d is designed as a smooth fifth order polynomial, but the initial and final times are the initial time of the first stage t_0 and the final time of the second stage t_2, respectively.

During the second stage, we desire that the probe follows the drogue positions along the Y_n and Z_n axis exactly. The reference trajectory is designed as a smooth transition between the mean drogue position (Y_d, Z_d) and the current drogue position $[y_d(t), z_d(t)]$, along the Y_n and Z_n axis, respectively. The smooth transition can be accomplished by a linear or higher-order interpolation. A fifth-order interpolation scheme gives very smooth transitions between the two stages. Let us consider tracking along the Y_n axis for simplicity. The reference trajectory using the fifth-order interpolation can be generated by the following equations:

$$y_r(t) = Y_d + \kappa y_d(t) \quad \text{if} \quad t > t_1 \quad \text{and} \quad t \le t_2 \tag{3}$$

where

$$\kappa = 10\tau^3 - 15\tau^4 + 6\tau^5 \tag{4}$$

and

$$\tau = (t - t_1)/(t_2 - t_1) \tag{5}$$

To ensure that the reference trajectory is feasible and does not demand excessive rates in the states as well as the control, the time durations of the first and second stages (t_1 and t_2) are design parameters that must be judiciously selected as functions of the initial offset (X_d, Y_d, Z_d).

The idea of dividing the reference trajectory generation into two stages also serves another purpose. The first stage does gross positioning and hence needs only an approximate location of the drogue mean position. Hence a GPS-based approximate measurement can be used for this purpose. During stage 2, accurate drogue position is needed, and the receiver aircraft is closer to the drogue. Hence VisNav measurements can be used, which become more accurate with reduction in range between the sensor and beacons.

IV. Observer for Estimating Reference States

The reference trajectory generated in Sec. III is expressed in terms of the outputs δX, δY and δZ, respectively. However, the controller that will be developed in Sec. V is a state feedback controller, which requires the knowledge of the full state vector for the reference trajectory. The purpose of the observer is to generate the reference states that the receiver aircraft should follow so that it can track the reference trajectory.

The plant is modeled as a linear-time-invariant state-space perturbation model, with the nominal trajectory being steady, level, 1-g trimmed flight:

$$\dot{\boldsymbol{x}}(t) = A\boldsymbol{x}(t) + B\boldsymbol{u}(t), \qquad \boldsymbol{y}(t) = C\boldsymbol{x}(t) \tag{6}$$

where $\boldsymbol{x}(t) \in \mathbb{R}^n$ is the state vector at time t; $A \in \mathbb{R}^{n \times n}$, $B \in \mathbb{R}^{n \times m}$, and $C \in \mathbb{R}^{r \times n}$ are the plant, control distribution, and output matrices, respectively; $\boldsymbol{u}(t) \in \mathbb{R}^m$ is the control vector; and $\boldsymbol{y}(t) \in \mathbb{R}^n$ are outputs that the controller is intended to track.

If the plant must follow the reference output $\boldsymbol{y}^*(t)$, then there exist states $\boldsymbol{x}^*(t)$ and controls $\boldsymbol{u}^*(t)$, such that

$$\dot{\boldsymbol{x}}^*(t) = A\boldsymbol{x}^*(t) + B\boldsymbol{u}^*(t), \qquad \boldsymbol{y}^*(t) = C\boldsymbol{x}^*(t) \tag{7}$$

The object is to estimate $\boldsymbol{x}^*$ and $\boldsymbol{u}^*$ from $\boldsymbol{y}^*$. In a conventional NZSP formulation this is achieved by assuming that the desired output $\boldsymbol{y}^*$ is constant. Thus the variables $\boldsymbol{x}^*$ and $\boldsymbol{u}^*$ are constants, and $\dot{\boldsymbol{x}}^* = 0$. Thus, Eq. (7) becomes

$$\begin{bmatrix} 0 \\ \boldsymbol{y}^* \end{bmatrix} = \begin{bmatrix} A & B \\ C & 0 \end{bmatrix} \begin{bmatrix} \boldsymbol{x}^* \\ \boldsymbol{u}^* \end{bmatrix} \tag{8}$$

Thus, $\boldsymbol{x}^*$ and $\boldsymbol{u}^*$ can be estimated by inverting Eq. (8)

$$\begin{bmatrix} \boldsymbol{x}^* \\ \boldsymbol{u}^* \end{bmatrix} = \begin{bmatrix} A & B \\ C & 0 \end{bmatrix}^{-1} \begin{bmatrix} 0 \\ \boldsymbol{y}^* \end{bmatrix} \tag{9}$$

For a time-varying trajectory the NZSP methodology can be used to approximately estimate $\boldsymbol{x}^*(t)$ and $\boldsymbol{u}^*(t)$ as

$$\begin{bmatrix} \boldsymbol{x}^*(t) \\ \boldsymbol{u}^*(t) \end{bmatrix} = \begin{bmatrix} A & B \\ C & 0 \end{bmatrix}^{-1} \begin{bmatrix} 0 \\ \boldsymbol{y}^*(t) \end{bmatrix} \tag{10}$$

By doing so, the state derivative $\dot{\boldsymbol{x}}^*(t)$ is neglected. To incorporate $\dot{\boldsymbol{x}}^*(t)$ in the estimation $\boldsymbol{x}^*(t)$ and $\boldsymbol{u}^*(t)$, we propose designing an output injection observer. Note that the atmospheric turbulence and wake effects are neglected in the observer while estimating the states $\boldsymbol{x}^*(t)$ and control $\boldsymbol{u}^*(t)$. The control estimated by the observer is the feedforward component of the control. In an ideal scenario, where the plant is modeled perfectly, the observer estimation is exact, and no atmospheric turbulence or vortex wake effects of the tanker are present, this feedforward component can cause the plant to track the desired reference trajectory exactly. When the just-mentioned uncertainties and disturbances are present in reality, the plant deviates from the desired reference trajectory. The feedback component of the control is introduced to accommodate the uncertainties and disturbances and reduce the deviations from the reference trajectory.

As already mentioned, the atmospheric turbulence and the wake effects are neglected in the observer. Moreover, the plant model in the observer is numerically propagated within the computer and is not subjected to physical disturbances or noise, making it deterministic.

Henceforth, we shall drop the t notation for simplicity and compactness. Let us define the new augmented state vector

$$\boldsymbol{X}^* = [\boldsymbol{x}^* \quad \boldsymbol{u}^*]^T \tag{11}$$

with derivative

$$\dot{\boldsymbol{X}}^* = \begin{bmatrix} \dot{\boldsymbol{x}}^* \\ \dot{\boldsymbol{u}}^* \end{bmatrix} = \begin{bmatrix} A & B \\ 0 & 0 \end{bmatrix} \begin{bmatrix} \boldsymbol{x}^* \\ \boldsymbol{u}^* \end{bmatrix} + \begin{bmatrix} 0 \\ I \end{bmatrix} \dot{\boldsymbol{u}}^* \tag{12}$$

in which 0 represents null matrices and I represents identity matrices of appropriate dimensions. Similarly, we define the output injection observer dynamics as

$$\dot{\hat{\boldsymbol{X}}} = \begin{bmatrix} \dot{\hat{\boldsymbol{x}}} \\ \dot{\hat{\boldsymbol{u}}} \end{bmatrix} = \begin{bmatrix} A & B \\ 0 & 0 \end{bmatrix} \begin{bmatrix} \hat{\boldsymbol{x}} \\ \hat{\boldsymbol{u}} \end{bmatrix} + L \left\{ \boldsymbol{y}^* - [C \quad 0] \begin{bmatrix} \hat{\boldsymbol{x}} \\ \hat{\boldsymbol{u}} \end{bmatrix} \right\} \tag{13}$$

where the augmented state vector $\hat{\boldsymbol{X}}$ for the observer is formed from the concatenation of $\hat{\boldsymbol{x}}$ and $\hat{\boldsymbol{u}}$:

$$\hat{\boldsymbol{X}} = [\hat{\boldsymbol{x}} \quad \hat{\boldsymbol{u}}]^T \tag{14}$$

Thus the state-space equations for the desired reference trajectory and the observer are

$$\dot{\boldsymbol{X}}^* = \mathcal{A}\boldsymbol{X}^* + \mathcal{B}\dot{\boldsymbol{u}}^*, \qquad \boldsymbol{y}^* = \mathcal{C}\boldsymbol{X}^* \tag{15}$$

$$\dot{\hat{\boldsymbol{X}}} = \mathcal{A}\hat{\boldsymbol{X}} + L\mathcal{C}(\boldsymbol{X}^* - \hat{\boldsymbol{X}}), \qquad \hat{\boldsymbol{y}} = \mathcal{C}\hat{\boldsymbol{X}} \tag{16}$$

where

$$\mathcal{A} = \begin{bmatrix} A & B \\ 0 & 0 \end{bmatrix}, \qquad \mathcal{B} = \begin{bmatrix} 0 \\ I \end{bmatrix}, \qquad \mathcal{C} = [C \quad 0] \tag{17}$$

Let $\boldsymbol{e}$ be the error between the desired and the observer states:

$$\boldsymbol{e} = \boldsymbol{X}^* - \hat{\boldsymbol{X}} \tag{18}$$

Differentiating Eq. (18) with respect to time and substituting Eqs. (15) and (16) we have

$$\dot{\boldsymbol{e}} = (\mathcal{A} - L\mathcal{C})\boldsymbol{e} + \mathcal{B}\dot{\boldsymbol{u}}^* \tag{19}$$

The observer gain L is selected to place the poles of $\mathcal{A} - L\mathcal{C}$ far enough in the left half of the s plane so that the estimation error vanishes quickly. The poles of $\mathcal{A} - L\mathcal{C}$ can be arbitrarily assigned to desired locations if and only if $(\mathcal{C}, \mathcal{A})$ is observable. The gain L that places the poles at the desired locations can be calculated using the dual of LQR theory[19] as

$$L = P_o \mathcal{C}^T R_o^{-1} \tag{20}$$

where P_o is a solution to the steady-state Ricatti equation

$$0 = \mathcal{A}P_o + P_o\mathcal{A}^T + Q_o - P_o\mathcal{C}^T R_o^{-1}\mathcal{C}P_o \tag{21}$$

The positive semidefinite matrix Q_o and positive-definite matrix R_o are the design parameters corresponding to the state and the output respectively. Note that Eq. (19) has an exponentially stable component $(\mathcal{A} - L\mathcal{C})\boldsymbol{e}$ and a bounded disturbance $\mathcal{B}\dot{\boldsymbol{u}}^*$. By proper choice of the poles of $\mathcal{A} - L\mathcal{C}$, the error $\boldsymbol{e}$ can be kept very small. Also, whenever $\dot{u}^*$ becomes zero the estimation error e tends to zero asymptotically.

V. Trajectory Tracking Controller Design

The reference observer estimates the desired states $\hat{\boldsymbol{x}}$ and controls $\hat{\boldsymbol{u}}$. In absence of uncertainty and disturbances, the feedforward control $\hat{\boldsymbol{u}}$ can track the desired reference trajectory accurately. A feedback controller must be designed to compensate for the trajectory errors arising as a result of the modeling uncertainties and external disturbances. We shall design a state feedback controller assuming that all of the states are available for feedback. This is usually not a restricting assumption for the case of a modern air vehicle because most or all of the states are usually measured.

The perturbation equation for the plant as seen in Eq. (6) is obtained by linearizing about the trim trajectory of steady level 1-g flight. This trim state does not include the gusts caused by turbulence or the vortex wake of the tanker aircraft. The disturbances caused by turbulence are stochastic but have zero mean. The disturbances caused by the tanker wake are constant with respect to time but vary with location. Whenever the receiver aircraft is in close proximity with the tanker, nonzero forces and moments will act on it because of the tanker wake. Thus zero perturbation states $\delta\boldsymbol{x} = 0$ are not equilibrium states in the presence of the tanker wake. Thus some control must be applied at zero perturbation to maintain the aircraft in equilibrium. A proportional controller of the form $\delta\boldsymbol{u} = -K_p\delta\boldsymbol{x}$ cannot achieve this as $\delta\boldsymbol{u}$ goes to zero whenever $\delta\boldsymbol{x}$ zero. So we incorporate integral action in the controller. An integrator can provide zero steady-state error for constant disturbances and constant reference trajectories. Even though these conditions are not met in the current problem, the integral action leads to a substantial reduction in the tracking error over a proportional controller. So we use a proportional-integral (PI) state feedback controller.

Let $\tilde{\boldsymbol{x}}$ be the error between the plant state and the desired state. Similarly, let $\tilde{\boldsymbol{u}}$ be the error between the control applied to the plant and the desired control.

$$\tilde{\boldsymbol{x}} = \boldsymbol{x} - \boldsymbol{x}^* \tag{22}$$

$$\tilde{\boldsymbol{u}} = \boldsymbol{u} - \boldsymbol{u}^* \tag{23}$$

Differentiating with respect to time and using Eqs. (6) and (7) results in

$$\dot{\tilde{\boldsymbol{x}}} = A\tilde{\boldsymbol{x}} + B\tilde{\boldsymbol{u}} \tag{24}$$

To incorporate integral action, let us define additional states $\boldsymbol{z} \in \mathbb{R}^3$ such that

$$\dot{\boldsymbol{z}} = \boldsymbol{y} - \boldsymbol{y}^* = C(\boldsymbol{x} - \boldsymbol{x}^*) = C\tilde{\boldsymbol{x}} \tag{25}$$

Consider the new augmented state vector

$$\mathbb{X} = [\boldsymbol{z} \quad \tilde{\boldsymbol{x}}]^T \tag{26}$$

The augmented state equation now becomes

$$\dot{\mathbb{X}} = \begin{bmatrix} \dot{\boldsymbol{z}} \\ \dot{\tilde{\boldsymbol{x}}} \end{bmatrix} = \begin{bmatrix} 0 & C \\ 0 & A \end{bmatrix} \begin{bmatrix} \boldsymbol{z} \\ \tilde{\boldsymbol{x}} \end{bmatrix} + \begin{bmatrix} 0 \\ B \end{bmatrix} \tilde{\boldsymbol{u}} = \mathbb{A}\mathbb{X} + \mathbb{B}\tilde{\boldsymbol{u}} \tag{27}$$

The state feedback control is calculated using the following equation:

$$\tilde{\boldsymbol{u}} = -\mathbb{K}\mathbb{X} \tag{28}$$

where $\mathbb{K}$ is an appropriate state feedback gain. Thus the closed-loop tracking error dynamics are

$$\dot{\mathbb{X}} = (\mathbb{A} - \mathbb{B}\mathbb{K})\mathbb{X} \tag{29}$$

The controller gain $\mathbb{K}$ is selected to place the poles of $\mathbb{A} - \mathbb{B}\mathbb{K}$ far enough in the left half of s plane so that the tracking error vanishes quickly. The poles of $\mathbb{A} - \mathbb{B}\mathbb{K}$ can be arbitrarily assigned to desired locations if and only if $(\mathbb{A}, \mathbb{B})$ is controllable. The gain $\mathbb{K}$ can be calculated using linear-quadratic-regulator theory as

$$\mathbb{K} = R_c^{-1}\mathbb{B}^T P_c \tag{30}$$

where P_c is the positive-definite solution to the steady-state Ricatti equation

$$0 = \mathbb{A}^T P_c + P_c \mathbb{A} + Q_c - P_c \mathbb{B} R_c^{-1} \mathbb{B}^T P \tag{31}$$

Here the positive-semidefinite matrix Q_c and the positive-definite matrix R_c are the weighting matrices on the states and the controls, respectively. Using Eqs. (28) and (26), the control can be written as

$$\tilde{\boldsymbol{u}} = -K_i z - K_p \tilde{\boldsymbol{x}} \tag{32}$$

where K_i and K_p are the integral and proportional submatrices of matrix gain K, of appropriate dimensions. From Eqs. (22), (23), and (32) we have the control law

$$\boldsymbol{u} = \boldsymbol{u}^* + K_p \boldsymbol{x}^* - K_p \boldsymbol{x} - K_i z \tag{33}$$

Because the desired states and controls are not known, the estimated states and controls are used.

$$\boldsymbol{u} = \hat{\boldsymbol{u}} + K_p \hat{\boldsymbol{x}} - K_p \boldsymbol{x} - K_i \hat{z} \tag{34}$$

where

$$\dot{\hat{z}} = C(\boldsymbol{x} - \hat{\boldsymbol{x}}) \tag{35}$$

Let us examine how the tracking error dynamics are affected if we use $\hat{\boldsymbol{x}}$ and $\hat{\boldsymbol{u}}$ instead of $\boldsymbol{x}^*$ and $\boldsymbol{u}^*$. Substituting Eqs. (34) and (23) in Eq. (29), we have

$$\dot{\mathbb{X}} = \mathbb{A}\mathbb{X} + \mathbb{B}(\hat{\boldsymbol{u}} + K_p \hat{\boldsymbol{x}} - K_p \boldsymbol{x} - K_i \hat{z}) \tag{36}$$

Adding and subtracting $\mathbb{B}K_p\boldsymbol{x}^*$ and $\mathbb{B}K_i z$ from the right-hand side of Eq. (36) results in

$$\dot{\mathbb{X}} = (\mathbb{A} - \mathbb{B}\mathbb{K})\mathbb{X} + [\mathbb{B}K_p \quad \mathbb{B}] \begin{bmatrix} \hat{\boldsymbol{x}} - \boldsymbol{x}^* \\ \hat{\boldsymbol{u}} - \boldsymbol{u}^* \end{bmatrix} + \mathbb{B}K_i(z - \hat{z}) \tag{37}$$

Note that the quantity $[\hat{\boldsymbol{x}} - \boldsymbol{x}^* \;\; \hat{\boldsymbol{u}} - \boldsymbol{u}^*]^T$ in Eq. (37) is by definition the estimation error vector $\boldsymbol{e}$. Defining

$$\zeta \triangleq z - \hat{z} \tag{38}$$

Differentiating Eq. (38) with respect to time, we have

$$\dot{\zeta} = [C \quad 0]\boldsymbol{e} \tag{39}$$

Thus ζ is the integral of the output estimation error. Combining Eqs. (37), (19), and (39), we have

$$\begin{bmatrix} \dot{\mathbb{X}} \\ \dot{\boldsymbol{e}} \\ \dot{\zeta} \end{bmatrix} = \begin{bmatrix} \mathbb{A} - \mathbb{B}\mathbb{K} & [\mathbb{B}K_p \quad \mathbb{B}] & \mathbb{B}K_i \\ 0 & \mathcal{A} - L\mathcal{C} & 0 \\ 0 & [C \quad 0] & 0 \end{bmatrix} \begin{bmatrix} \tilde{\boldsymbol{x}} \\ \boldsymbol{e} \\ \zeta \end{bmatrix} + \begin{bmatrix} 0 \\ \mathcal{B} \\ 0 \end{bmatrix} \dot{\boldsymbol{u}}^* \tag{40}$$

Here we see that the estimation error dynamics is independent of the tracking error, and the separation principle holds. Thus the observer and the controller can be designed separately, and the stability properties are retained if the systems are combined. The combined system is exponentially stable with bounded disturbance from the term $\dot{\boldsymbol{u}}^*$. By proper choice of the poles of $\mathbb{A} - \mathbb{B}\mathbb{K}$ and $\mathcal{A} - L\mathcal{C}$, the estimation error $\boldsymbol{e}$ and tracking error $\mathbb{X}$ can be kept very small. Also, whenever $\dot{\boldsymbol{u}}^*$ becomes zero the estimation error and the tracking error tend to zero asymptotically.

VI. Frequency-Domain Stability Robustness and Performance Robustness Analysis

Figure 6 is a system block diagram representation of the entire sensor-navigation-control algorithm. Here $\boldsymbol{n}_1$ is the VisNav sensor noise, $\boldsymbol{n}_2$ is the aircraft state feedback sensor noise, $\boldsymbol{n}_3$ is the error in measuring the inertial position of the receiver aircraft, $\boldsymbol{n}_4 = \boldsymbol{n}_1 + \boldsymbol{n}_3$, w are the winds gusts, and $\boldsymbol{\Delta d}$ are the perturbations caused by high-frequency unmodeled dynamics. The VisNav sensor measures the relative position vector between the receiver aircraft and the drogue, along with some VisNav measurement noise. Thus the output of the sensor is $\boldsymbol{y}_d - \boldsymbol{y} + \boldsymbol{n}_1$. Therefore, to get the drogue inertial position, the receiver aircraft position must be added to the VisNav measurement. The receiver aircraft inertial position is measured with some measurement noise, and the resultant signal is $\boldsymbol{y} + \boldsymbol{n}_3$. When this signal is added to the VisNav measurement, the $-\boldsymbol{y}$ and $+\boldsymbol{y}$ cancel each other out, showing that the overall system does not have a feedback of the receiver aircraft position y. The resultant signal fed to the trajectory generation module $\boldsymbol{y}_d + \boldsymbol{n}_1 + \boldsymbol{n}_3$, consists of only the drogue inertial position, the error in measurement of drogue inertial position, and the VisNav sensor noise, which are independent of the receiver aircraft inertial position $\boldsymbol{y}$. The output of the trajectory generation module $\boldsymbol{y}^* + \boldsymbol{n}_4$ is also independent of $\boldsymbol{y}$.

On performing block diagram reduction on Fig. 6 subfigure 1, subfigure 2 is obtained. In subfigure 2 of Fig. 6, consider the region between the marked points A and B. The input to this part $\boldsymbol{y}^* + \boldsymbol{n}_4$ is independent of the output $\boldsymbol{y}$. Also this part has all linear elements, so that an equivalent transfer function can be obtained. Note that the trajectory generation module, which is the nonlinear element, is prior to point A. For the system robustness analysis we analyze the system block diagram only between points A and B.

Equation (41) shows the total dynamics between the desired reference trajectory and the plant output.

$$\begin{bmatrix} \dot{\hat{\boldsymbol{x}}} \\ \dot{\hat{\boldsymbol{u}}} \\ \dot{\boldsymbol{x}} \\ \dot{z} \end{bmatrix} = \begin{bmatrix} A - L_1 C & B & 0 & 0 \\ -L_2 C & 0 & 0 & 0 \\ BK_p & B & A - BK_p & -BK_i \\ -I & 0 & I & 0 \end{bmatrix} \begin{bmatrix} \hat{\boldsymbol{x}} \\ \hat{\boldsymbol{u}} \\ \boldsymbol{x} \\ z \end{bmatrix}$$

$$+ \begin{bmatrix} L_1 \\ L_2 \\ 0\,0 \end{bmatrix} (\boldsymbol{y}^* + \boldsymbol{n}_4) - \begin{bmatrix} 0 \\ 0 \\ BK_p \\ 0 \end{bmatrix} \boldsymbol{n}_2 + \begin{bmatrix} 0 \\ 0 \\ G \\ 0 \end{bmatrix} w + \begin{bmatrix} 0 \\ 0 \\ I \\ 0 \end{bmatrix} \boldsymbol{\Delta d} \tag{41}$$

The stability and performance robustness can be analyzed by looking at the multi-input/multi/output (MIMO) bode magnitude plot of singular values for the transfer function between the various inputs and the plant output.

From Eq. (41) we see that the transfer function from the reference trajectory to the plant output is the same as the transfer function between the VisNav sensor noise and the plant output. Thus the singular values of the transfer function should be shaped so that they are equal to 0 dB at low frequencies, for the reference to be tracked accurately, and the singular values should be low at high frequencies so that VisNav sensor noise is rejected. Figure 7a indicates that the plant can accurately track reference trajectories up to 0.5 rad/s and reject VisNav sensor noise at 100 Hz (=314 rad/s). Figure 7b shows that the singular value plot of the transfer function between the state feedback sensor noise and the plant output has a smooth roll-off at high frequencies, as desired, and rejects the feedback sensor noise above 100 rad/s. The singular values show a decrease of 20 dB/decade at low frequencies indicating good rejection of any sensor bias. Figure 7c, subplot 2 is the wind gust spectral density and shows that the disturbance is active at frequencies below

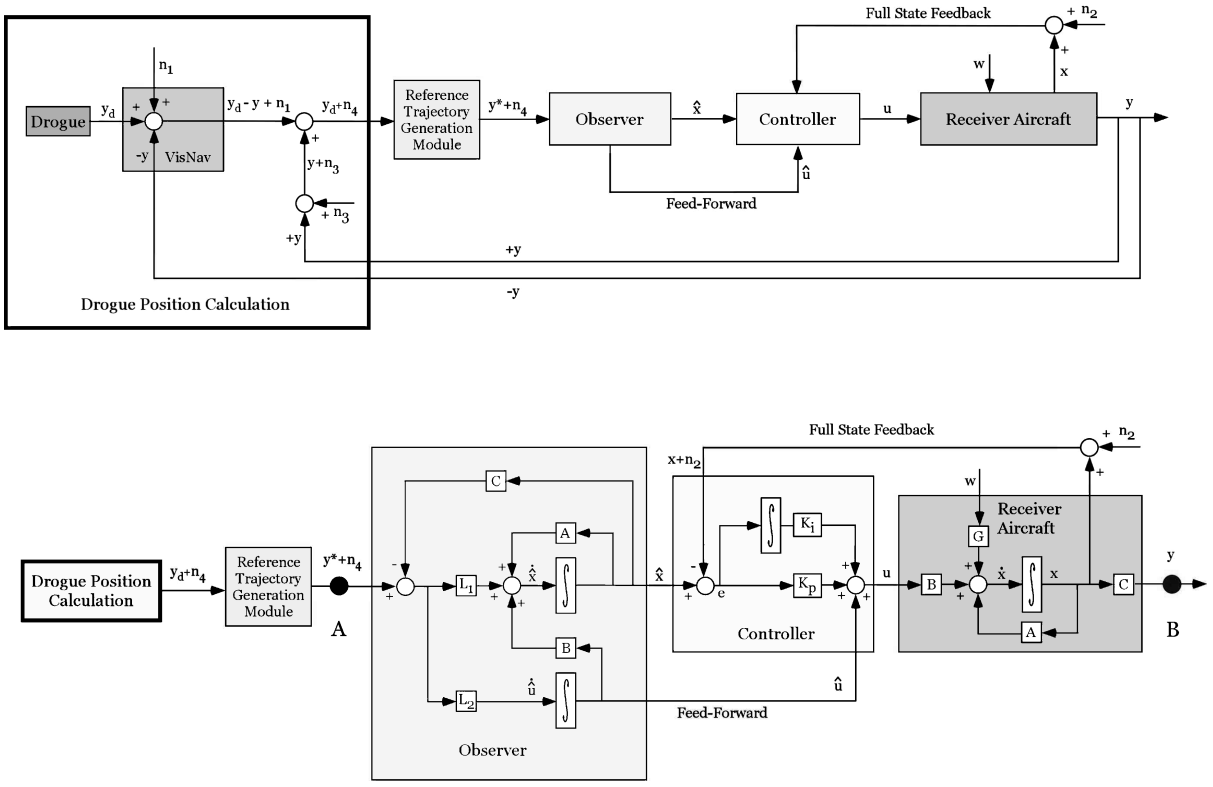

Fig. 6 Block diagram of sensor-navigation-control system.

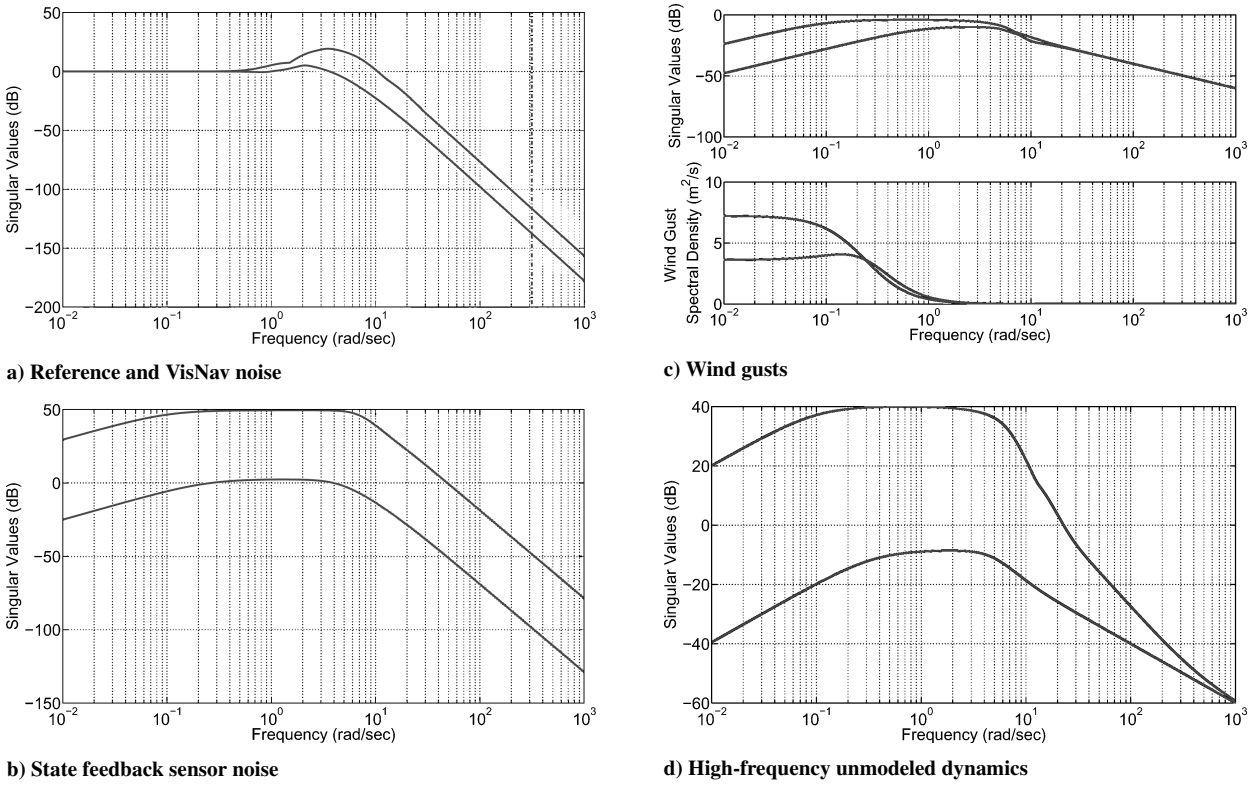

a) Reference and VisNav noise

c) Wind gusts

b) State feedback sensor noise

d) High-frequency unmodeled dynamics

Fig. 7 MIMO bode magnitude plot of singular values for the transfer function between the various inputs and the plant output.

1 rad/s. From Fig. 7c, subplot 1 we see that the maximum singular value of the transfer function between the wind gust and the plant output is less than 0 dB. Also, the singular values have a roll off of 20 dB/decade at low frequencies showing robustness to low-frequency disturbances caused by wind gusts. Disturbances caused by the tanker vortex wake are a low frequency phenomenon and the addition of an integrator in the controller provides good robustness at low frequencies. Figure 7d indicates robustness to high-frequency unmodeled dynamics above 50 rad/s. Based on these results, the total system is judged to possess stability robustness and performance robustness for the specific uncertainties and disturbances considered.

VII. Numerical Examples

The objective of the simulation is to investigate the feasibility of the combined sensor and control system for fully autonomous unmanned tanker-unmanned receiver aircraft probe-and-drogue air

Table 1 Receiver aircraft modeling uncertainty

Derivative	Uncertainty, %
C_{L_α}	5
C_{m_α}	10
C_{l_β}	20
C_{n_β}	15
C_{l_p}	15
$C_{l_\delta a}$	5
$C_{l_{\delta r}}$	5
$C_{m_{\delta e}}$	5
$C_{m_{\delta pwr}}$	5
$C_{n_{\delta a}}$	5
$C_{n_{\delta r}}$	5

refueling. The refueling scenario considered in the test case consists of both the tanker and receiver aircraft flying in steady, level, 1-g flight, with the same velocity and the same heading. The receiver aircraft is in formation but 30 m behind, 15 m to the right, and 15 m below the drogue suspended from the tanker aircraft. The task for the receiver aircraft is to close with the tanker and dock the fuel probe tip with the drogue receptacle.

The numerical simulation of the receiver aircraft used in the example is a linear model of an unmanned air vehicle called UCAV6. It is a 60% scale AV-8B Harrier aircraft with the pilot and all pilot support devices removed, with the mass properties and aerodynamics adjusted accordingly. For the simulations presented here, all thrust-vectoring capability was disabled. The linear model of UCAV6 is described in detail in the appendix. A detailed VisNav simulation model is integrated with the receiver aircraft simulation to account for realistic effects such as noise characteristics, estimate convergence, processing times, effect of sampling times, beacons falling out of sensor field of view, sensor range considerations, etc. The drogue motion is simulated by a six-degrees-of-freedom, second-order spring mass damper model. The parameters of the model are selected to replicate the motion of the drogue as seen from the videos of aerial refueling.

Both the receiver aircraft and the drogue are subjected to turbulence appropriate for the flight conditions of the test, generated with the Dryden gust model. A rms turbulence intensity of 3 ft/s true airspeed (TAS) was selected to generate light turbulence at the test altitude of 6000 m (Ref. 20).

A simplified wake vortex model[21–23] is introduced in the simulation to model the aerodynamic coupling between the tanker and the receiver aircraft in close proximity. The aerodynamic model of the tanker wing is represented by a horseshoe wing vortex, and the velocities induced on the receiver aircraft are calculated. These velocities form a spatial flow field that varies with the location, but is constant with respect to time. The stochastic component is already modeled by the turbulence. The aerodynamic loads on the receiver aircraft as a result of the induced velocities are calculated for various sections of the receiver aircraft wing, and these loads are integrated over the entire wing to estimate the total forces and moments on the receiver aircraft. The position of the drogue is considered at an offset of 10 m to the right with respect to the tanker centerline longitudinal axis to aggravate the asymmetric disturbance effects caused by the tanker wake.

The observer and the controller are designed by using a nominal receiver aircraft model. Uncertainty in the receiver aircraft dynamical model is addressed by randomly introducing errors into the most significant stability derivatives in the A matrix and in all of the control derivatives in the B matrix, during numerical simulation. Table 1 lists these derivatives and the applied uncertainties that result from using analytical methods, as reported by Roskam.[24] No uncertainty is introduced into the kinematic constraint relationships since they are exact. Finally, a low-pass actuator model was used to simulate the actuator dynamics.

A. Reference-Observer-Based Tracking Controller

Figure 8a shows the receiver aircraft following the smooth spline trajectory as seen from the reference frame, which is steady, level, 1-g flight. Note that all of the following subfigures are of perturbation variables from steady state. Figure 8b shows the time histories of the linear reference states generated by the observer and the resulting tracking performance of the controller. The controller is seen to follow the states δX, δY, and δZ generated by the observer very closely, culminating in a successful docking. The plant does not closely follow the observer for the states δv and δw. This is because the observer states are estimated without considering the disturbances caused by the tanker vortex wake. When the receiver aircraft motion is simulated in close proximity to the tanker, the plant states deviate from the observer states as a result of the vortex wake. Figure 8c shows the time histories of the angular states, and Fig. 8d shows the time histories of the aerodynamic angles. The angular perturbations seen in both of the figures are very small because the controller is trying to track a smooth spline trajectory. These small excursions of the perturbation variables from the steady-state values validate the linear model assumption for this problem. Figure 8e shows that control deflections and rates are well within maximum bounds.

The projection of the probe and drogue trajectories in the $Y_n - Z_n$ plane (Fig. 8f) shows how well the receiver aircraft is able to follow the the smooth spline trajectory and reach the estimated mean drogue position. Note especially the accurate tracking during stage 2, as the probe slowly converges to the drogue position in the $Y_n - Z_n$ plane. Figure 9a shows the tracking error of the probe trip with respect to the drogue. The radius tracking error is defined as the distance between the probe tip and the center of the drogue, projected into the $Y_n - Z_n$ plane. When the probe tip is in close proximity to the drogue along the X_n axis, the radius tracking is about 5 cm. Figure 9b summarizes a series of closed-loop docking simulations in which the Dryden turbulence amplitude was gradually increased from 0 to 10 ft/s TAS (light to severe) under ideal visibility conditions. The docking simulation was run 50 times for each value of turbulence intensity. Successful docking was defined as when the probe tip is within a 0.1-m radius of the refueling port at zero range. Figure 9c shows the docking radius error for 50 runs at each turbulence intensity from 0 to 10 ft/s TAS, and Fig. 9d shows the average value and 3σ limits for the same.

B. VisNav Sensor Performance Characteristics

This section addresses sensor specific performance issues of measurement errors, beacon drop-outs, and docking success rates. A detailed model of the VisNav sensor[1] was incorporated into the AAR system developed in this paper to examine the behavior of the sensor in a closed-loop docking environment. Figure 10a shows the time histories of the VisNav measurement errors.The VisNav sensor model includes realistic field-of-view constraints and a representation of the beacon energy drop-off behavior caused by range effects and visibility conditions. In the sensor model the ideal measured voltages from the PSD are corrupted with Gaussian noise. To emulate optical distortion effects, measurements closer to the periphery of the sensor receive noise with a higher variance than those in the center. The simulated voltages are passed through a nonlinear calibration function that determines the coordinates of the light centroid on the photodiode and thus the measured line-of-sight vector to the beacon. Tests are performed before and after the calibration process to check the validity of the measurements. Measurements from a particular beacon are discarded if 1) the light centroid does not fall within the calibrated area of the photodiode, and this occurs when the beacon is not in the sensor's field of view; and 2) the energy from the light centroid is too low to be detected by the sensor, and the energy of a simulated measurement is a function of range, visibility conditions, and beacon size.

When measurements from a beacon satisfy one of the preceding criteria, the beacon is considered to have dropped out of the field of view, and those measurements are not passed to the estimation routine. The GLSDC routine is capable of producing an updated estimate with as few as four beacons, but even with multiple beacons the loss of one or more can in certain situations affect the continuity of the solution (see Fig. 10b). When fewer than four beacons are visible, there is logic in the sensor to return the last good estimate

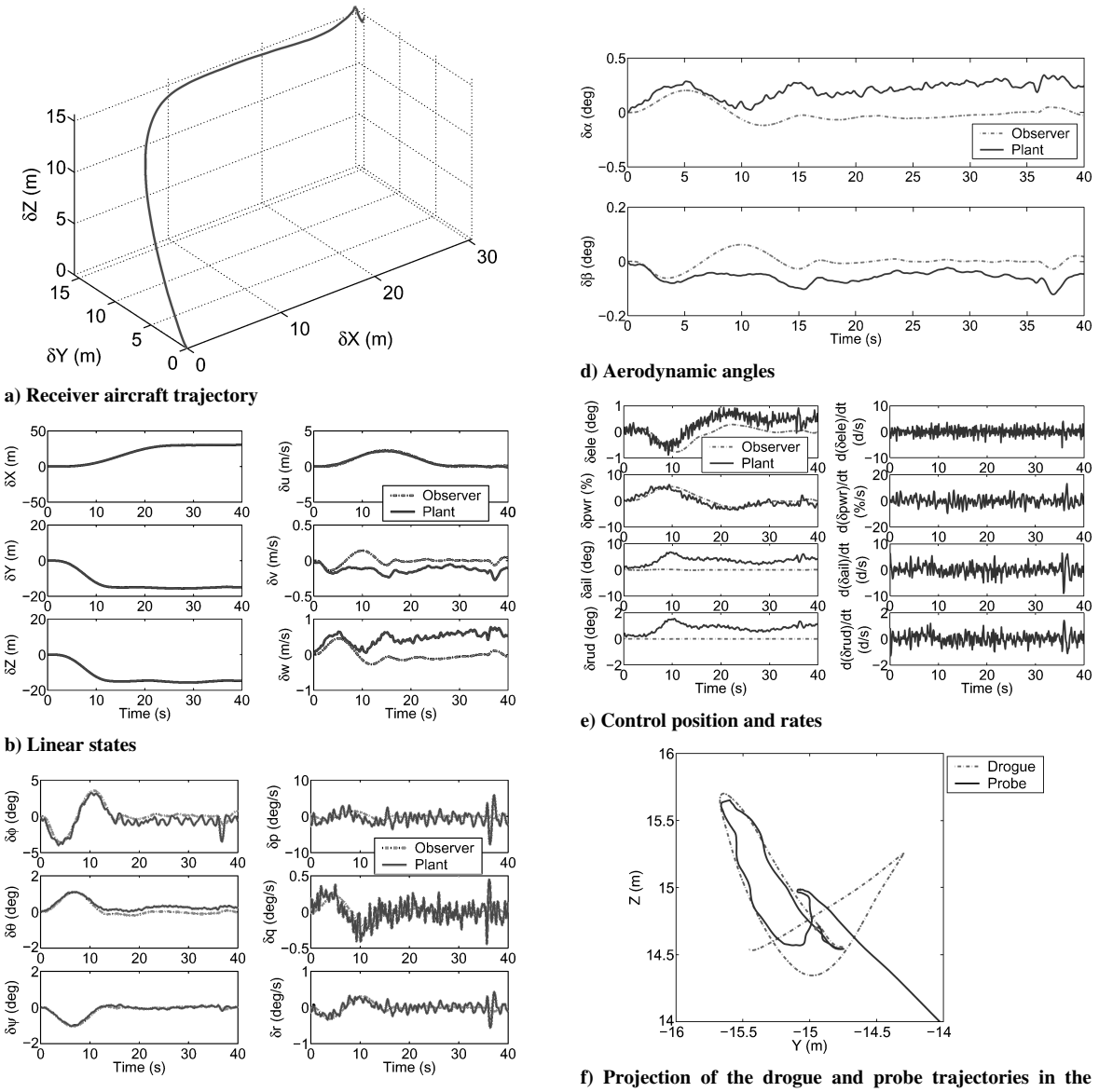

Fig. 8 Time histories of the plant trajectory variables.

and an increased error covariance. Future work will explore the use of a Kalman filter to provide estimates in this case.

Beacon drop-out is most likely to occur when disturbances cause the beacons to move outside the sensor field of view as the sensor approaches the active beacon array. In the simulation using the realistic sensor model, light to moderate turbulence levels were seen to cause intermittent beacon drop-outs during the final docking stage, beginning when the receiver is about 10 m from the drogue. Figure 10b shows an example of what can happen to the VisNav estimation error when one or more beacons drop out of the field of view. Spikes in the solution can occur, but in most cases the solution is recovered when the beacons move back into the field of view. As the turbulence intensity is increased, the solution is less likely to converge once several beacons have dropped out. In addition, the large, high-frequency variations in the navigation solution from VisNav have a detrimental effect on closed-loop performance, causing the controller to overcompensate and saturate the receiver aircraft controls.

The phenomenon shown in Fig. 10b is not caused by the number of beacons approaching the critical value of four. The GLSDC routine will produce accurate measurements with as few as four beacons as long as 1) the beacons are spaced properly in three dimensions and 2) the measurement model is correct. Figure 10b illustrates a case for which the measurement model was incorrect because the inverse calibration was not properly accounted for. When a beacon light centroid moves into the outer regions of the PSD, the lens distortion causes a displacement from the location predicted by the ideal pinhole camera model. This distorted measurement should not have been included in the set of measurements in GLSDC, but because it was, it caused the estimate to degrade. Proper calibration prevents this effect. Not shown in the figure are the error covariances (3-σ bounds) that do not enclose the spikes in the solution. As features leave the field of view of the sensor, the 3-σ bounds will reflect a change in the confidence of the estimate. Thus when the number of features is reduced by one, the error covariances increase slightly, but the estimate continues to converge.

It is clear that the field of view of the VisNav sensor will be application dependent, and based on these results the field of view used for these investigations will continue to be modified. Two other approaches considered to mitigate the effect of intermittent beacon drop-out are Kalman filtering to smooth the estimates and thereby reduce the saturation effect on the controller and active stabilization of the drogue. The former can be easily incorporated into the present system.

C. Comparison of Baseline and Improved Controllers

The tracking performance of the proportional-integral nonzero set point controller with control rate weighting (PI-NZSP-CRW)[1] is compared to the proportional-integral reference-observer-based

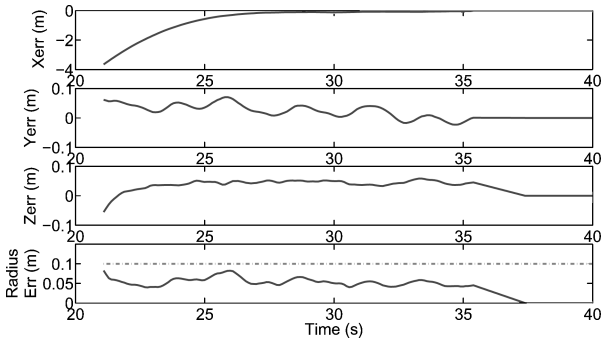

a) Tracking errors for σ gust = 3

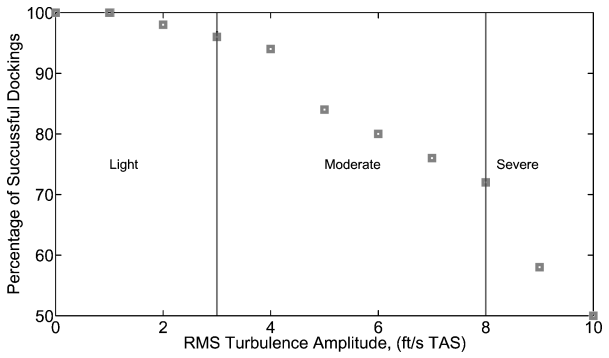

b) Docking success rates in various turbulence levels

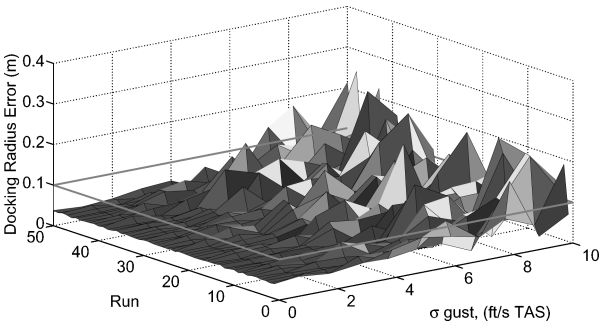

c) Docking success rates in various turbulence levels

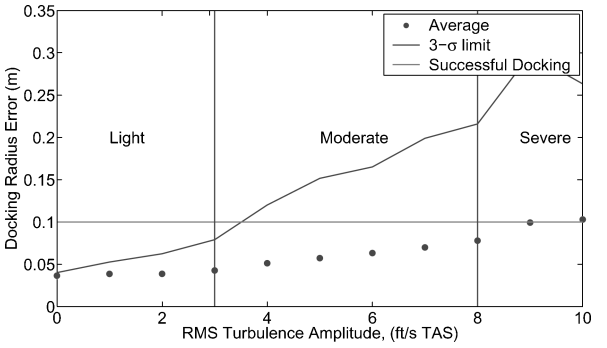

d) Docking success rates in various turbulence levels

Fig. 9 Tracking errors and turbulence study.

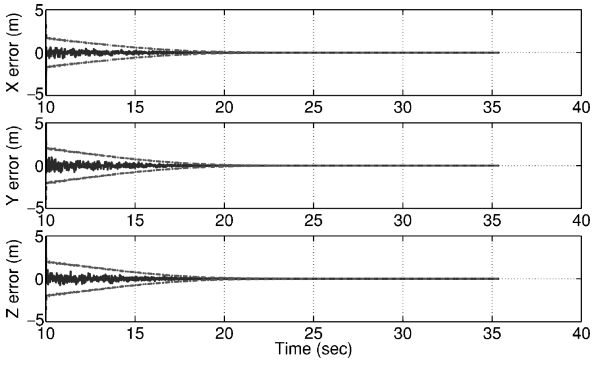

a) VisNav measurement error and 3-σ bounds

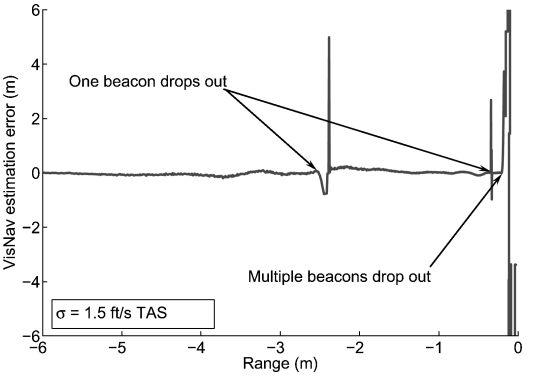

b) VisNav estimation error with beacon drop-out in Dryden light turbulence σ gust = 1.5

Fig. 10 High-fidelity sensor simulation performance results.

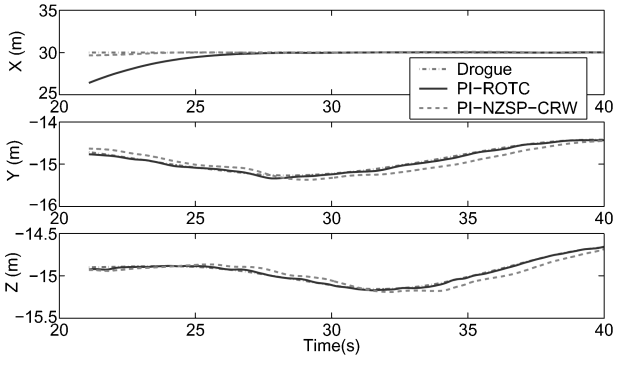

a) Tracking performance

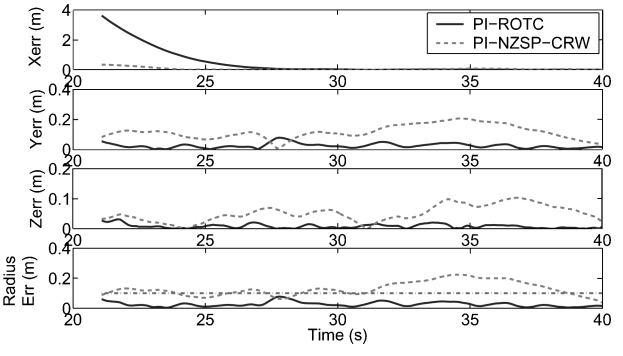

b) Tracking error

Fig. 11 Comparison between PI-NZSP-CRW and PI-ROTC controller.

tracking controller (PI-ROTC) developed in this paper for the same refueling condition, using similar gains for both the controllers. Considering first the PI-NZSP-CRW controller, Fig. 11a shows that the probe tip trajectory lags behind the drogue trajectory. This is expected because the PI-NZSP-CRW controller assumes a steady drogue position and neglects the state derivative $\dot{\boldsymbol{x}}^*(t)$ while estimating $\boldsymbol{x}^*(t)$ and $\boldsymbol{u}^*(t)$. This is explained in detail in Sec. IV. The PI-ROTC controller incorporates the state derivative $\dot{\boldsymbol{x}}^*(t)$ in the estimation process and hence does not exhibit significant lag in the tracking performance. Compared to the PI-NZSP-CRW controller, Fig. 11b shows that the ROTC controller produces a 75% decrease in the tracking error.

VIII. Conclusions

This paper developed a reference-observer-based tracking Controller designed for integration with an existing vision-based sensor system, for fully autonomous aerial refueling between an unmanned tanker aircraft and an unmanned receiver aircraft using the probe-and-drogue method. Using measurements from the vision-based sensor, a smooth spline trajectory from the receiver aircraft initial position to the position of a moving drogue was generated. The unique aspect about this paper is that it uses a reference observer to estimate the open-loop feedforward control and the reference states that the plant needs to follow, to track a reference trajectory generated onboard the aircraft in real time. A full-state feedback controller was designed to ensure that the plant accurately tracks the states generated by the observer. A stability and robustness analysis was performed, and numerical simulation results was presented for the cases of light to severe turbulence, with the presence of tanker vortex wake effects on the receiver aircraft. The impact of sensor measurement errors and beacon drop-outs on docking success rates was presented, and a direct comparison between the trajectory tracking controller developed in this paper and an earlier proportional-integral nonzero Setpoint–control rate weighting controller was conducted. Based on the results presented in the paper, the following is concluded:

1) The integrated observer and controller system is exponentially stable with bounded disturbance from the term $\dot{\boldsymbol{u}}^*$. By proper choice of the poles of the closed loop for the observer and the controller, the estimation error $\boldsymbol{e}$ and tracking error $\tilde{\boldsymbol{x}}$ can be kept very small.

2) Frequency-domain robustness analysis shows that the system has both stability robustness and performance robustness to uncertainties and disturbances consisting of VisNav sensor noise, state feedback sensor noise from sensors on the receiver aircraft, light turbulence caused by wind gusts, and high-frequency unmodeled dynamics.

3) Numerical simulation results demonstrate that the integrated observer and controller system are able to effectively track and dock with a nonstationary drogue. Tracking error was reduced by 75%, and the probe tip could be maintained within a 5-cm radius circle of the center of the drogue in the presence of light turbulence and disturbances caused by the tanker vortex wake.

Extensions of this work will incorporate a high-fidelity model of the flowfield effects of the tanker aircraft instead of a simplified model used currently. Current efforts are directed to develop a more accurate model of the drogue dynamics. The current model is a hypothetical second-order spring mass damper model that closely replicates the drogue motions observed in videos of actual docking. Solutions to the discontinuities in the VisNav solutions caused by beacon dropouts will be investigated. Careful selection of the sensor field of view will reduce the occurrence of beacon drop-outs, and a Kalman filter estimator will be incorporated to reduce their effect by smoothing the measurements. Current drogue designs are passively aerodynamically stabilized and therefore experience large displacement motions in moderate to severe levels of turbulence. An actively controlled drogue to enable docking in higher levels of turbulence is also being investigated. Finally, work is currently underway for a flight-test demonstration of the vision sensor and controller developed in this paper for both an air-to-ground refueling demonstration, and a subsequent air-to-air refueling demonstration.

Appendix: Receiver Aircraft Linear Model

The linear model is obtained by linearizing about steady level flight. The trim values are angle of attack $\alpha_0 = 4.35$ deg, trim velocity $V_0 = 128.7$ m/s, trim elevator deflection $ele_0 = 7.5$ deg, and the trim engine power input $pwr_0 = 55\%$. The state vector is

$$x = [\delta X \quad \delta Y \quad \delta Z \quad \delta u \quad \delta v \quad \delta w \quad \delta p \quad \delta q \quad \delta r \quad \delta\phi \quad \delta\theta \quad \delta\psi] \tag{A1}$$

$$A = \begin{bmatrix}
0 & 0 & 0 & 0.99 & 0 & 0.0759 & 0 & 0 & 0 & 0 & 0 & 0 \\
0 & 0 & 0 & 0 & 1 & 0 & 0 & 0 & 0 & -32.06 & 0 & 422.2 \\
0 & 0 & 0 & -0.07 & 0 & 0.99 & 0 & 0 & 0 & 0 & -422.2 & 0 \\
0 & 0 & 0 & -0.03 & 0 & 0.16 & 0 & -31.99 & 0 & 0 & -32.02 & 0 \\
0 & 0 & 0 & 0 & -0.33 & 0 & 31.9 & 0 & -418 & 32.02 & 0 & 0 \\
0 & 0 & 0 & -0.06 & 0 & -1.34 & 0 & 409.5 & 0 & 0 & -2.43 & 0 \\
0 & 0 & 0 & 0 & -0.02 & 0 & -3.64 & 0 & 1.72 & 0 & 0 & 0 \\
0 & 0 & 0 & 0 & 0 & -0.02 & 0 & -0.77 & 0 & 0 & 0 & 0 \\
0 & 0 & 0 & 0 & 0.02 & 0 & -0.21 & 0 & -1.19 & 0 & 0 & 0 \\
0 & 0 & 0 & 0 & 0 & 0 & 1 & 0 & 0.07 & 0 & 0 & 0 \\
0 & 0 & 0 & 0 & 0 & 0 & 0 & 1 & 0 & 0 & 0 & 0 \\
0 & 0 & 0 & 0 & 0 & 0 & 0 & 0 & 1.003 & 0 & 0 & 0
\end{bmatrix}$$

where $\delta()$ are the perturbations from the steady-state values, and the steady-state is assumed as steady level 1-g flight. Here, δX, δY, δZ are perturbations in the inertial positions; δu, δv, δw are perturbations in the body-axis velocities; $\delta p, \delta q, \delta r$ are perturbations in the body-axis angular velocities; and $\delta\phi, \delta\theta, \delta\psi$ are perturbations in the Euler attitude angles.

The control variables δele-elevator, $\delta \%pwr$-percentage power, δail-aileron, and δrud-rudder are perturbations in the control effectors from the trim values. The control vector is

$$u = \begin{bmatrix} \delta ele & \delta \%pwr & \delta ail & \delta rud \end{bmatrix} \tag{A2}$$

$$B = \begin{bmatrix}
0 & 0 & 0 & 0 \\
0 & 0 & 0 & 0 \\
0 & 0 & 0 & 0 \\
0.0081 & 0.2559 & 0 & 0 \\
0 & 0 & -0.2945 & 0.4481 \\
0.2772 & 0.2286 & 0 & 0 \\
0 & 0 & 0.5171 & 0.0704 \\
0.1164 & 0.0143 & 0 & 0 \\
0 & 0 & 0.0239 & -0.0895 \\
0 & 0 & 0 & 0 \\
0 & 0 & 0 & 0 \\
0 & 0 & 0 & 0
\end{bmatrix} \tag{A3}$$

Acknowledgments

This research is supported by StarVision Technologies Incorporated, under Grant Number 04-0792. The technical monitor is Brian O. Wood. This support is gratefully acknowledged by the authors. The authors thank Jeffrey C. Morris for contributions to the VisNav sensor simulation model, Lance W. Traub for contributions to the tanker wake vortex model, and Kenneth M. Edwards of the Air Force Research Laboratory AFRL/MNAV for his many insights and suggestions. Finally, the authors wish to thank the reviewers for their many insightful comments and suggestions that improved the paper.

References

[1]Valasek, J., Gunnam, K., Kimmett, J., Tandale, M. D., Junkins, J. L., and Hughes, D., "Vision-Based Sensor and Navigation System for Autonomous Air Refueling," *Journal of Guidance, Control, and Dynamics*, Vol. 28, No. 5, 2005, pp. 832–844.

[2]Nalepka, J. P., and Hinchman, J. L., "Automated Aerial Refueling: Extending the Effectiveness of Unmanned Air Vehicles," AIAA Paper 2005-6005, Aug. 2005.

[3]John, J., Deyst, J. P. H., and Park, S., "Lyapunov Stability of a Nonlinear Guidance Law for UAVs," AIAA Paper 2005-6230, Aug. 2005.

[4]Campa, G., Seanor, B., Perhinschi, M., Fravolini, M., Ficola, A., and Napolitano, M., "Autonomous Aerial Refueling for UAVs Using a Combined GPS-Machine Vision Guidance," AIAA Paper 2004-5350, Aug. 2004.

[5]Fravolini, M., Ficola, A., Napolitano, M., Campa, G., and Perhinschi, M., "Development of Modeling and Control Tools for Aerial Refueling for UAVs," AIAA Paper 2003-5798, Aug. 2003.

[6]Stepanyan, V., Lavretsky, E., and Hovakimyan, N., "Aerial Refueling Autopilot Design Methodology: Application to F-16 Aircraft Model," AIAA Paper 2004-5321, Aug. 2004.

[7]Pachter, M., Houpis, C. H., and Trosen, D. W., "Design of a Air-to-Air Automatic Refueling Flight Control System Using Quantitative Feedback Theory," *International Journal of Robust and Nonlinear Control*, Vol. 7, No. 6, 1997, pp. 561–580.

[8]Pollini, L., Innocenti, M., and Mati, R., "Vision Algorithms for Formation Flight and Aerial Refueling with Optimal Marker Labeling," *Collection of Technical Papers—AIAA Modeling and Simulation Technologies Conference*, Vol. 1, AIAA, Reston, VA, 2004, pp. 208–220.

[9]Valasek, J., Kimmett, J., Hughes, D., Gunnam, K., and Junkins, J. L., "Vision Based Sensor and Navigation System for Autonomous Aerial Refueling," AIAA Paper 2002-3441, May 2002.

[10]Kimmett, J., Valasek, J., and Junkins, J. L., "Autonomous Aerial Refueling Utilizing A Vision Based Navigation System," AIAA Paper 2002-4469, Aug. 2002.

[11]Kimmett, J., Valasek, J., and Junkins, J. L., "Vision Based Controller for Autonomous Aerial Refueling," *Proceedings of the IEEE Control Systems Society Conference on Control Applications*, Vol. 2, IEEE Publications, Piscataway, NJ, 2002.

[12]Andersen, C. M., "Three Degree of Freedom Compliant Motion Control For Robotic Aircraft Refueling," Master's Thesis, Aeronautical Engineering, Air Force Inst. of Technology, AFIT/GAE/ENG/90D-01, Wright–Patterson, OH, 13 Dec. 1990.

[13]Bennett, R. A., "Brightness Invariant Port Recognition For Robotic Aircraft Refueling," Master's Thesis, Electrical Engineering, Air Force Inst. of Technology, AFIT/GE/ENG/90D-04, Wright–Patterson, OH, 13 Dec. 1990.

[14]Shipman, R. P., "Visual Servoing For Autonomous Aircraft Refueling," Master's Thesis, Air Force Inst. of Technology, AFIT/GE/ENG/89D-48, Wright–Patterson, OH, Dec. 1989.

[15]Abidi, M. A., and Gonzalez, R. C., "The Use of Multisensor Data for Robotic Applications," *IEEE Transactions on Robotics and Automation*, Vol. 6, No. 2, 1990, pp. 159–177.

[16]Lachapelle, G., Sun, H., Cannon, M. E., and Lu, G., "Precise Aircraft-to-Aircraft Positioning Using a Multiple Receiver Configuration," *Proceedings of the National Technical Meeting, Institute of Navigation*, Institute of Navigation, Alexandria, VA, 1994, pp. 793–799.

[17]Kimmett, J. J., "Autonomous Aerial Refueling of UAVs Utilizing a Vision Based Navigation System," Master's Thesis, Aerospace Engineering, Texas A&M Univ., College Station, TX, Aug. 2002.

[18]Junkins, J. L., Hughes, D. C., Wazni, K. P., and Pariyapong, V., "Vision-Based Navigation for Rendezvous, Docking, and Proximity Operations," *Advances in the Astronautical Sciences*, Vol. 101, Elsevier, Inc., Burlington, MA, 1999, pp. 203–220.

[19]Lewis, F. L., and Syrmos, V. L., *Optimal Control*, 2nd ed., Wiley-Interscience, New York, 1995, pp. 161–173.

[20]"Military Specification: Flying Qualities of Piloted Aircraft," Mil-f-8785c, IHS, Inc., Englewood, CO, Nov. 1980.

[21]Dogan, A., Venkataramanan, S., and Blake, W., "Modeling of Aerodynamic Coupling Between Aircraft in Close Proximity," *Journal of Aircraft*, Vol. 42, No. 4, 2005, pp. 941–955.

[22]Bloy, A. W., and Trochalidis, V., "Aerodynamic Interference Between Tanker and Receiver Aircraft During Air-to-Air Refuelling," *Aeronautical Journal*, Vol. 95, No. 935, May 1990, p. 165.

[23]Traub, L. W., "Theoretical and Experimental Investigation of Biplane Delta Wings," *Journal of Aircraft*, Vol. 38, No. 3, 2001, pp. 536–546.

[24]Roskam, J., *Airplane Flight Dynamics and Automatic Flight Controls*, Vol. 1, Design, Analysis, and Research Corp., Lawrence, KS, 1994, p. 236.